JOURNAL OF GEOPHYSICAL RESEARCH, VOL. 112, B02203, doi:10.1029/2005JB003883, 2007

Click Here for Full Article

Generation of fine hydromagmatic ash by growth and disintegration of glassy rinds

Larry G. Mastin[1]

Received 10 June 2005; revised 7 August 2006; accepted 29 August 2006; published 21 February 2007.

[1] The deposits of mafic hydromagmatic eruptions are more fine grained and variable in vesicularity than dry magmatic deposits. Blocky, equant shapes of many hydromagmatic clasts also contrast with droplet, thread, and bubble wall morphology of dry magmatic fragments. Small (<~180 μm), blocky hydromagmatic pyroclasts have traditionally been interpreted to result from discrete vapor explosions, although such explosions tend to occur only under certain conditions. This paper considers a process of hydromagmatic ash formation that involves repeated growth and disintegration of glassy rinds on pyroclast surfaces as they deform within turbulent flows. This process, termed "turbulent shedding", may occur during the expansion phase of vapor explosions or during turbulent but nonexplosive mixing of magma with water, steam, or water sprays. The occurrence of turbulent shedding and the resulting fragment sizes depend on the timescale for rind growth and the timescale between disturbances that remove or disintegrate glassy rinds. Turbulent shedding is directly observable in some small littoral jets at Kilauea. Calculations suggest that, in the presence of liquid water or water sprays, glassy rinds having a thickness of microns to millimeters should form in milliseconds to seconds. This is similar to the timescale between turbulent velocity fluctuations that can shred lava globules and remove such rinds. The fraction of a deposit consisting of fine ash should increase with the duration of this process: Large-scale Surtseyan jets generate hundreds or thousands of shedding events; bubble bursts or tephra jets at Kilauea's coast may produce only a few.

Citation: Mastin, L. G.(2007), Generation of fine hydromagmatic ash by growth and disintegration of glassy rinds, J. Geophys. Res., *112*, B02203, doi:10.1029/2005JB003883.

1. Introduction

[2] The textural and grain size differences between basaltic pyroclasts of hydromagmatic or Surtseyan origin and those of dry Strombolian or Hawaiian eruptions have been widely studied since the early 1970s [*Heiken*, 1972; *Walker and Croasdale*, 1972; *Waters and Fisher*, 1971]. *Walker and Croasdale* [1972] pointed out that fragments of the former are "bounded by fracture surfaces", whereas those of the latter have "an external form in part controlled by surface tension". Although other clast morphologies also exist in hydromagmatic deposits [*Wohletz*, 1983], equant, blocky fragments with fracture-bound surfaces remain one of the most distinguishing features of basaltic hydromagmatism. Other distinguishing features are fine average grain size and relatively poor sorting [*Fisher and Schmincke*, 1984; *Walker*, 1971; *Walker and Croasdale*, 1972]; Surtseyan deposits typically have median grain sizes less than 1 mm even in the most proximal locations whereas median diameters of Strombolian or Hawaiian lava fountain deposits may range up to centimeters or more.

[3] The morphology and grain size characteristics of hydromagmatic deposits have generally been interpreted in the context of discrete vapor explosions [*Buettner et al.*, 1999; *Morrissey et al.*, 2000; *Wohletz*, 1983; *Zimanowski*, 1998], sometimes referred to as fuel coolant interactions (FCI) or molten fuel coolant interactions (MFCI). FCI's involve breakup and heat transfer of any hot melt when mixed with cooler, vaporizable liquid [*Corradini*, 1991]; MFCI's are a type of FCI in which the vaporizable liquid is water [*Zimanowski*, 1998]. These terms were first used in studying the origin of extremely violent explosions involving water and liquid metals, and many authors [*Buchanan*, 1974; *Buchanan and Dullforce*, 1973; *Buettner et al.*, 2002; *Fisher and Schmincke*, 1984, pp. 80–81; *Peckover et al.*, 1973; *Sheridan and Wohletz*, 1983; *Zimanowski et al.*, 1997b] state or imply that the term fuel coolant interaction is synonymous with "vapor explosion". Others [*Morrissey et al.*, 2000; *Wohletz*, 1986] use the term FCI to denote any mixing process between a hot melt and vaporizable liquid, whether explosive or not.

[4] The interpretation that fine, blocky hydroclasts result from vapor explosions stems from the fact that many (although not all) directly observed Surtseyan-type eruptions [*Moore*, 1967; *Morimoto*, 1960; *Richards*, 1959] eject

[1]Cascades Volcano Observatory, U. S. Geological Survey, Vancouver, Washington, USA.

This paper is not subject to U.S. copyright.
Published in 2007 by the American Geophysical Union.

debris in transient pulses, termed "intermittent explosions" by *Thorarinsson* [1967]. *Colgate and Sigurgeirsson* [1973] and *Peckover et al.* [1973] suggested that these phenomena were analogous to vapor explosions recognized in industrial settings [*Bradley and Witte*, 1972; *Buchanan and Dullforce*, 1973; *Witte et al.*, 1970]. Several experimental projects have since investigated the role of vapor explosions in hydrovolcanism [*Buettner and Zimanowski*, 1998; *Trigila and Battaglia*, 2003; *Wohletz and McQueen*, 1984; *Zimanowski et al.*, 1997a; *Zimanowski et al.*, 1991].

[5] Industrial vapor explosions have generated shock waves, broken windows miles away, and killed or injured many workers at steel mills and aluminum foundries [*Witte et al.*, 1970]. The metals in such explosions are hot enough that, upon contacting water, a continuous vapor film rapidly develops at the interface, insulating the two materials for several seconds before the interface temperature decreases into the nucleate boiling range. Explosions require either that liquid water be heated metastably above the boiling point and then homogeneously nucleate; or that vapor films somehow collapse, forcing liquid water and metal into direct contact [*Corradini*, 1991; *Wohletz*, 1986]. Experimental and theoretical studies in the 1970s and 1980s showed that most vapor explosions involved the following mixing sequence [*Board et al.*, 1974; *Board et al.*, 1975; *Corradini*, 1991; *Patel and Theofanus*, 1978]: (1) Metals entering water form a coarse dispersal of melt blobs, each surrounded by vapor; (2) a pressure wave, generated externally or spontaneously, strips off vapor jackets and forces liquid water into direct contact with the melt; (3) vapor bubbles at the interface rapidly expand beyond the thermal boundary layer into cold water, then violently collapse, causing fluid instabilities that break up the meltwater interface; (4) continued bubble growth and collapse thoroughly fragments the melt, leading to explosive heat transfer and steam expansion. In water-magma systems Zimanowski and coworkers have generated explosions using a slightly different sequence in which an isolated pocket of water, injected into a volume of magma, is disrupted by shooting a projectile into the container [*Zimanowski*, 1998; *Zimanowski et al.*, 1997a]. In both metal- and magma-water systems the explosion trigger, or thermal detonation, is a pressure wave that collapses the insulating vapor film. Thermal detonation occurs over milliseconds or less and the following explosion generates powerful shock waves [*Witte et al.*, 1970; *Zimanowski et al.*, 1997b].

[6] *Wohletz* [1983], *Wohletz and McQueen* [1984], and *Morrissey et al.* [2000] suggested that blocky shapes of natural hydroclasts result from the rapid generation and collapse of vapor films during thermal detonation. *Wohletz* [1986] compared the wavelength of fluid instabilities during vapor collapse with hydromagmatic fragment size. *Zimanowski et al.* [1997b] suggested that blocky shards less than ~180 mm in diameter ("interactive" particles) were remnants of magma directly in contact with water at the time of detonation. *Buettner et al.* [2002, 1999] noted the occurrence of fine, angular hydroclasts from Vulcano that resemble particles generated in experimental vapor explosions. They also quantified clast shapes using the products of circularity times elongation and rectangularity times compactness, finding this second product higher in brittlely fragmented particles than in ductilely fragmented ones.

[7] Although thermal detonation associated with vapor film collapse may cause fine hydromagmatic fragmentation in some circumstances, it may not be the only cause. Thermal detonation occurs under conditions that are difficult to reproduce even in the laboratory. Increases in ambient pressure, melt viscosity, and volume fraction of noncondensable gases tend to suppress detonation [*Corradini*, 1991]. Highly vesicular melt has not been successfully detonated in the laboratory [*Zimanowski et al.*, 1995]. Moreover, magma that mixes with water vapor in an atmospheric plume is not surrounded by a continuous vapor film and therefore cannot detonate by the above mechanism.

[8] The limitations of laboratory-generated thermal detonation need not exclude the possibility of natural explosions by other, as yet undescribed mechanisms. As acknowledged by investigators (B. Zimanowski and K. Wohletz, personal communication), natural vapor explosions may be less transient or powerful than those in the laboratory and could be (probably are) localized at certain places and times within a magma-water mixture. Some such "explosions" may appear indistinguishable from vigorous, turbulent mixing driven by external momentum inputs. Nevertheless the possibility for fine hydromagmatic fragmentation in the absence of discrete explosions seems great enough to ask whether other mechanisms could be involved.

[9] In this regard it is relevant to point out that nearly all scenarios that generate fine hydromagmatic ash bear two common characteristics: (1) They involve turbulence that shreds magma and generates new hot surfaces; and (2) they immerse magma in steam, liquid water, or water sprays, that rapidly cool clast surfaces. In vapor explosions, intense turbulence and rapid cooling are coupled and self-propagating. In other natural settings, turbulence may result from external momentum inputs whereas cooling rate is influenced by the temperature, velocity, and water content of the ambient fluid.

[10] Turbulent mixing is important for its ability to rapidly deform magma and create new surface area that transfers heat from magma. Slow lava flows create little surface area per unit time whereas turbulent jets or (especially) vapor explosions can increase magma surface area by orders of magnitude in less than a second (Figure 1). Surface cooling rates range from nearly zero for magma entrained in hot gas to more than 10^6 K s^{-1} during vapor film collapse [*Zimanowski et al.*, 1997b] or droplet impact (discussed later). When deformation rates are high but cooling rates are low (e.g., a turbulent lava fountain), lava is shredded but then relaxes by surface tension before the surface can solidify (Figure 2a). Resulting fragments are droplet or thread shaped, or agglutinated. When cooling rates are high but deformation rates are low (e.g., in pillow lavas), thermal contraction fractures develop but the resulting fragments do not separate until detached by some disturbance such as wave action or downslope failure. Resulting fragments are angular and coarse.

[11] When deformation and cooling rates are both high, as for example in turbulent flows or in the expansion phase following thermal detonation, one might expect thin glassy rinds to grow on clast surfaces while the magma continues to deform in a fluid manner. Rapid deformation cannot be accommodated by the outer glassy rinds, which are hypothesized to peel, shatter, and regenerate on new clast surfaces

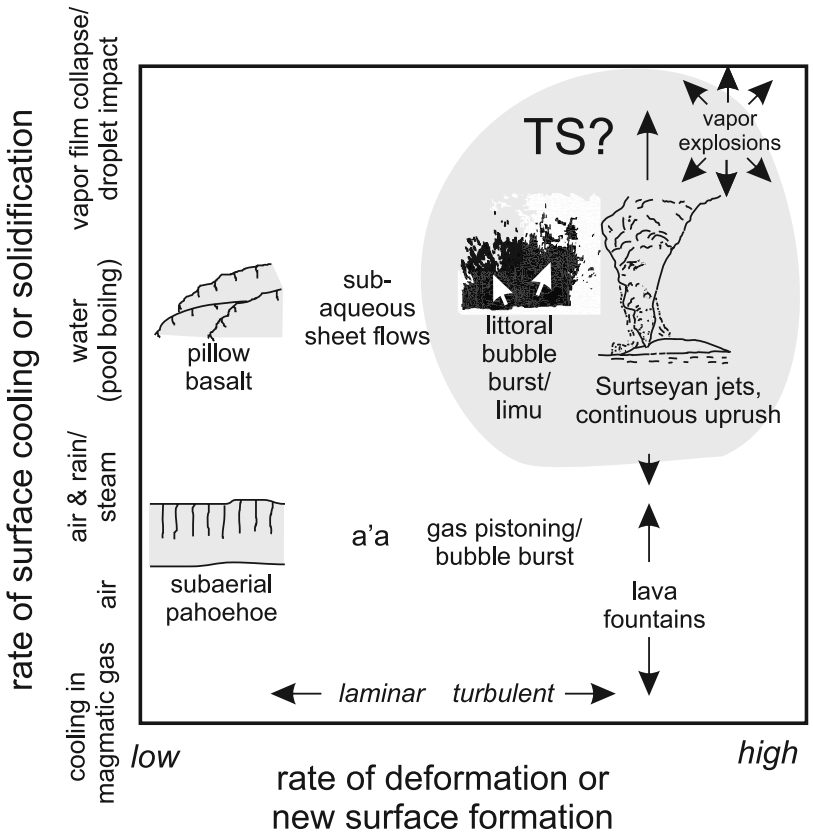

Figure 1. Schematic illustration of the range of rates of surface cooling and of deformation or new surface formation in natural volcanic flows and the kind of volcanic phenomena associated with these rates in low-viscosity magmas. The shaded area in the upper right labeled "TS?" is the region under which turbulent shedding is hypothesized to be important.

(Figure 2b). Thin filaments and sheets of melt may also quench and shatter like limu [*Hon et al.*, 1988] or, if not completely solidified, adhere to neighboring fragments that solidify together. The growth and disintegration of glassy fragments under these circumstances is referred to in this paper as "turbulent shedding."

[12] Glassy rind formation, fracture, and hydrodynamic breakup have been mentioned in previous volcanology papers [*Wohletz*, 1983, 1986; *Wohletz et al.*, 1989], primarily in the context of vapor explosions, but their combined effects have not been examined in detail. A key objective of this paper is to estimate the range of cooling and deformation rates that might be expected in natural hydromagmatic jets or sprays, and compare them with rates in which turbulent shedding might be important.

2. Observations of Magma-Water Interaction and Its Products

[13] In rare circumstances turbulent shedding has been directly observed along the coastline of Kilauea volcano, Hawaii. Figure 3 shows the ejection of lava from a submerged skylight at sea level. The expelled lava breaks up turbulently while its outer margin is cooled by air, water, or water vapor. The color of the lava surface reflects variations in temperature due to age and cooling rate. The darker skin is nearly solid, cannot stretch to accommodate the high deformation rate, and in places peels away from the rest of the lava body (white arrows) to form separate flakes that disintegrate during flight and upon impact. In the photo, the visible skins are perhaps millimeters thick and formed over seconds (perhaps longer if cooling began before ejection). Assuming a 1-m diameter lava bubble that expanded to a few meters in several tenths of a second, the average extensional strain rate is several per second but could be much higher locally. This case of turbulent shedding, however vivid, involves rates of deformation that are relatively low compared with high-speed turbulent flows.

[14] Figure 4a illustrates a more intense but very brief and less easily observable tephra jet type interaction at Kilauea. These jets occur when lava enters the surf through ruptured lava tubes, is torn apart by wave action, quenched, and thrown back on the beach as loose fragments that form small littoral cones [*Mattox and Mangan*, 1997]. Fragments from one such cone (Figure 4b), located at 19.33119°N, 155.04887°W (Old Hawaiian Datum), collected on 26 March 1999, are shown in Figures 4c–4i. As described by *Mattox and Mangan* [1997], most clasts from these cones have fluidal outer surfaces (Figures 4c and 4e) formed by surface tension. Many have fractured ends ("1", Figure 4c) that imply coarse brittle shattering after solidification. Submillimeter-sized clasts (Figure 4d) typically have flake shapes like limu ("2") [*Hon et al.*, 1988] or irregular, angular shapes ("3") that suggest fracture after solidifica-

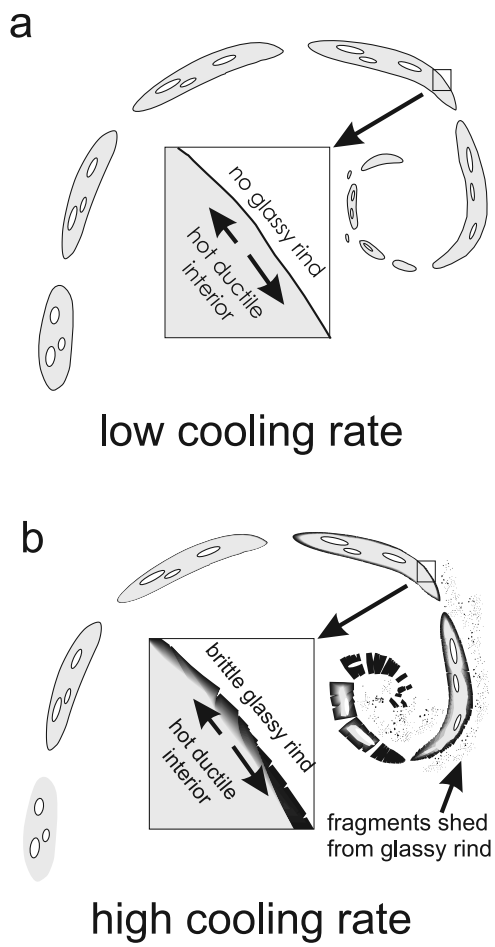

Figure 2. (a) Breakup of a low-viscosity lava globule in a turbulent eddy by viscous stretching and surface tension under low cooling rate. (b) Breakup of the same lava globule by viscous stretching and turbulent shedding under high cooling rate.

tion. At high magnification some clasts have fine particles adhering to them ("4", Figure 4e) as well as flakes or rinds ("5" through "11", Figures 4e–4i) a few to a few tens of micrometers thick, which are partially detached. With a few exceptions (Figure 4i) flakes are fresh and clean with no evidence of surface alteration that might reflect a hydration origin. The surface in Figure 4g, for example, is smooth down nearly to the micron scale. In Figure 4h, flakes are superimposed on linear ridges ("9") that resemble stretch marks observed in industrial glasses [e.g., *Sharma et al.*, 2003, Figure 4]. On littoral fragments these stretch marks are not throughgoing but are interrupted by patches of relatively smooth glass ("10") and flakes that may have cooled by droplet impact and therefore could not expand. By comparison, nonhydromagmatic fragments of 1959 Kilauea Iki lava fountain tephra from Kilauea's summit (Figures 5a–5c) also exhibit fluidal textures (Figure 5a) but their outer surfaces lack obvious flakes or rinds (Figures 5b and 5c). Stretch marks are apparent in Figure 5b, although with slightly different morphology than in Figure 4h.

[15] We interpret the textures on these littoral clasts to have formed from the following sequence. (1) Within the first few tenths of a second of wave impact, high cooling and deformation rates caused the growth of glassy rinds and their removal as clasts deformed. (2) During the following several seconds, clasts flew through clouds of steam and water vapor and continued cooling; but deformation rates slowed dramatically as clast size decreased, turbulence intensity decreased, and the partially cooled clast surfaces became resistant to deformation. (3) Upon landing the littoral clasts were mostly solid. Breakage of clast ends likely occurred upon landing or perhaps during sample collection (if they were already weakened by cooling fractures). Submillimeter-sized angular and limu-shaped clasts likely formed in the first few seconds as lava globules stretched out to sheets or filaments, solidified, and shattered.

[16] By this sequence, the thin, partially detached flakes and the submillimeter limu- and angular-shaped clasts would have resulted from the simultaneous cooling and deformation processes referred to in this paper as turbulent shedding. The remnant flakes (e.g., "6" in Figure 4f) have the angularity and size of interactive clasts associated with vapor explosions [*Buettner et al.*, 1999; *Zimanowski et al.*, 1997a]; and in concurrence with those studies, we interpret the these flakes to have formed at the instant of contact when cooling and deformation rates were highest. The scarcity and thinness of partially detached flakes on these particles however implies that rapid surface cooling was brief and operated to different degrees on each clast depending on the abundance of liquid water along each clast's flight path.

[17] On the basis of photographs and videos, we estimate ejection velocities in such jets to be several meters per second. If the flakes were truly glass ($T < \sim 1000$ K) at the time of quenching, cooling rates in the first few tenths of a second must have been several hundred degrees per second or greater. Deformation rates or, in quantitative terms, extensional strain rates can only be surmised but were probably several per second or greater at the moment these particles detached from the lava body.

3. Cooling Processes and Rates

[18] In this section we estimate the range of surface cooling rates of erupting magma on the basis of known processes and experimental results. Surface heat loss occurs by radiation, convection or conduction. The addition of water to the ambient fluid may increase the cooling rate by orders of magnitude depending on the properties of the liquids and the nature of the interaction. Figure 6 illustrates the possible range using measurements from previous studies and calculations described below.

3.1. Heat Loss by Radiation

[19] The rate of heat loss by radiation (q_{rad}) from a magma surface to surrounding fluid is:

$$q_{rad} = e\sigma_b\left(T_{mi}^4 - T_a^4\right) \tag{1}$$

where e is emissivity, σ_b is the Stefan-Boltzmann constant, T_a is the temperature of the ambient atmosphere, and T_{mi} is the temperature of the magma's outer surface (see Table 1 for a list of variables). Measured emissivities for solidified basalt are 0.90–0.95 [*Kahle et al.*, 1988; *Salisbury and D'Aria*, 1994] but ~0.55–0.75 for fluid basalt [*Abtahi et*

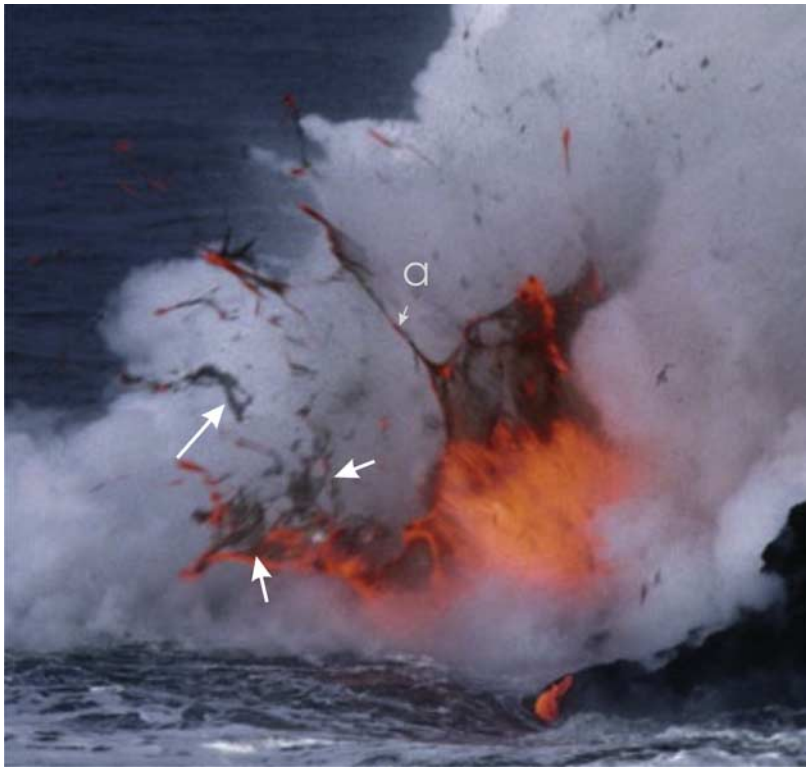

Figure 3. A bubble burst from a lava tube at Kilauea's shoreline illustrates the simultaneous cooling and breakup of magma during turbulent mixing with water and steam. Visible lava has been hurled upward in a fraction of a second, stretching the outer surface to several times its original length and exposing a new, hot, incandescent surface. Different parts of the lava surface have cooled to different degrees depending on their age and degree or nature of water contact. Blackish lava near the top is cooler and more viscous than the incandescent red and yellow surfaces, cannot sustain rapid deformation, and peels away to expose new, hot surface below. Some of the black fragments on the left side of the photo (white arrows) appear to be remnants of the peeled rind. Width of the photo is about three meters. USGS photo by T. J. Takahashi, 10 February 1988.

al., 2002; *Burgi et al.*, 2002]. For T_a = 25°C, e = 0.75, and T_{mi} above the glass transition (shaded region in Figure 6), radiative heat flux is about 30–200 kW m^{-2} (Figure 6).

3.2. Heat Loss by Convection

[20] When air is the ambient fluid, the rate of convective heat loss (q_{conv}^{air}) is generally given by:

$$q_{conv}^{air} = h(T_{mi} - T_a) \tag{2}$$

where the heat transfer coefficient h ranges from about 6 to 300 W m^{-2} K^{-1} depending on hydrodynamic conditions [*Kreith and Bohn*, 1986, Table 1.4, equation (7.10)]; above cooling pahoehoe flows under wind conditions of several meters per second h has been measured at ~45–50 W m^{-2} K^{-1} [*Keszthelyi and Harris*, 2003]. Using h = 50 W m^{-2} K^{-1} in (2) yields a rate of heat loss in the range of tens of thousands of Watts per square meter (Figure 6, bold dashed line). At interfacial temperatures below the glass transition (shaded region), convective heat loss by air generally exceeds radiative heat loss whereas the reverse is true above the glass transition temperature.

[21] The effect of water on convective heat loss (q_{conv}^{water}) depends greatly on water temperature, surface properties and hydrodynamic conditions [*Kreith and Bohn*, 1986, chapter 10]. Under pool-boiling conditions in which the interface lies within a pool of liquid water whose temperature is at the boiling point (Figure 6, bold solid line), q_{conv}^{water} ranges up to about 1 MW m^{-2}, with the highest value, known as the critical heat flux (CHF), at a surface temperature (T_{mi}) of 130–150°C. As surface temperature increases above ~150°C (the transition boiling regime), vapor bubbles increasingly insulate the interface and decrease the rate of heat loss to a minimum value known as the Leidenfrost point (LFP), at T_{mi} = 275–375°C. At higher surface temperature (the film boiling regime) a continuous vapor film separates the heated surface from liquid water and q_{conv}^{water} increases monotonically with temperature, reaching about 600 kW m^{-2} at T_{mi} = 1100°C.

[22] Several conditions can enhance the rate of heat loss above that for pool boiling. "Subcooling" the water below the boiling temperature can increase the critical heat flux to several megawatts per square meter (Figure 6, triangles) and raise the Leidenfrost temperature as vapor bubbles at the interface expand into cooler water and then violently

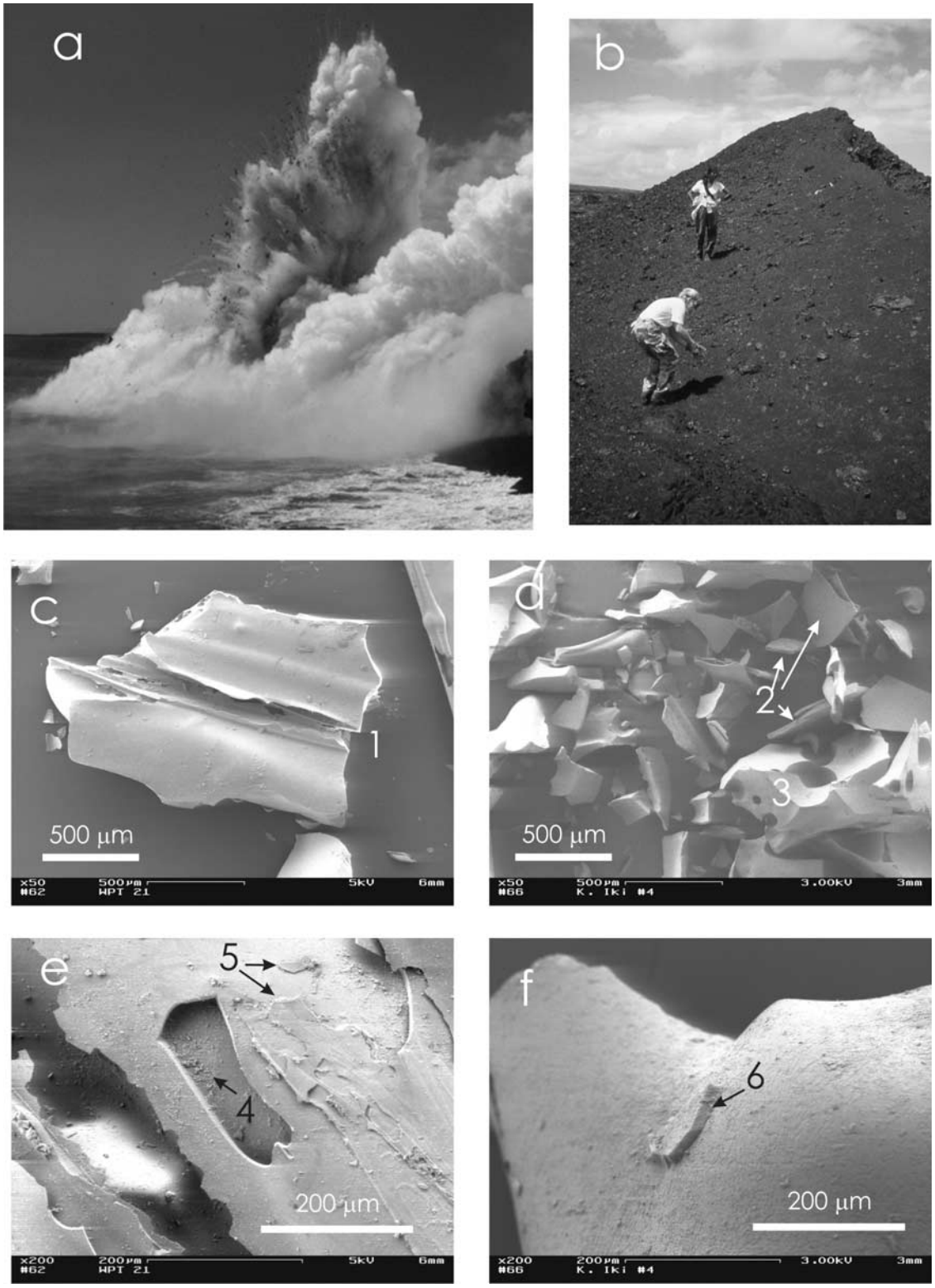

Figure 4. (a) A tephra jet at Kilauea's coastline (USGS photo by J. D. Griggs, 3 February 1988); (b) littoral cone at Kilauea's south coast formed by tephra jet activity; (c–i) Textures of clasts collected from the littoral cone in Figure 4b.

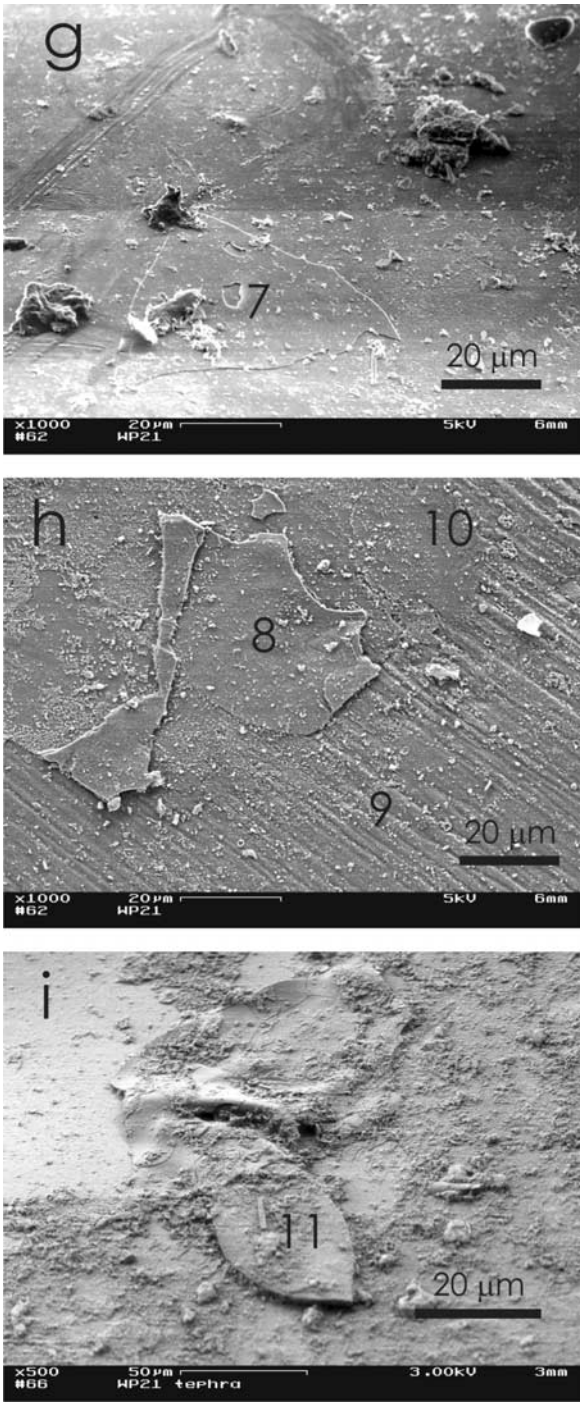

Figure 4. (continued)

collapse. Spraying subcooled (T_a = 25°C) water onto hot surfaces (T_{mi} > ~150°C) yields cooling rates of ~0.1–1.5 MW m^{-2} (light dotted lines with crosses) depending on water mass flow rate, droplet size, and impact velocity [*Bernardin and Mudawar*, 1997; *Bernardin et al.*, 1997; *Klinzing et al.*, 1992]. Water jets impacting hot surfaces under film-boiling conditions (bold dot-dashed lines) can yield heat loss rates more than 10 MW m^{-2} depending on impact velocity, surface temperature, and water temperature [*Liu and Wang*, 2001].

3.3. Heat Loss by Conduction

[23] Conduction is the dominant cooling mechanism over very brief periods of time when liquid water is in direct contact with the magma surface. Extreme rates of conductive heat transfer are known to be associated with vapor film collapse [*Wohletz*, 1983; *Zimanowski*, 1998] but also occur for a period of milliseconds after water droplets impact surfaces that are hotter than the Leidenfrost temperature (Figure 7c) [e.g., *Bernardin et al.*, 1997; *Bradfield*, 1966]. The period of direct liquid contact after droplet impact is much longer than the time to vaporize the water adjacent the surface, suggesting that some nonequilibrium pressure transient or kinetic nucleation delay maintains the water in liquid form. *Bolle and Moureau* [1982] estimate that more

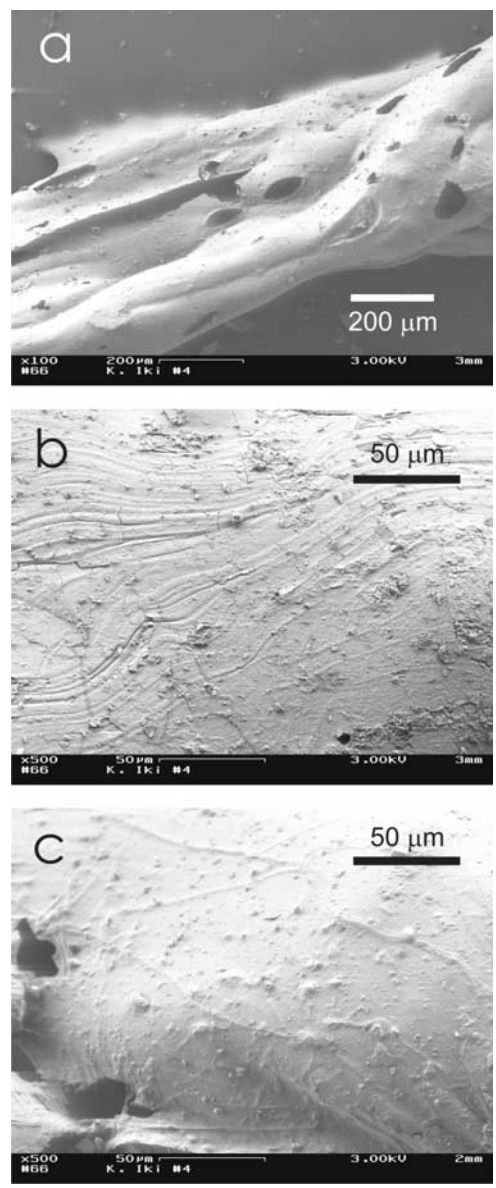

Figure 5. Images of tephra from the 1959 Kilauea Iki eruption collected 2.4 km SW of the eruptive vent along the dispersal axis. Annotations are explained in the text.

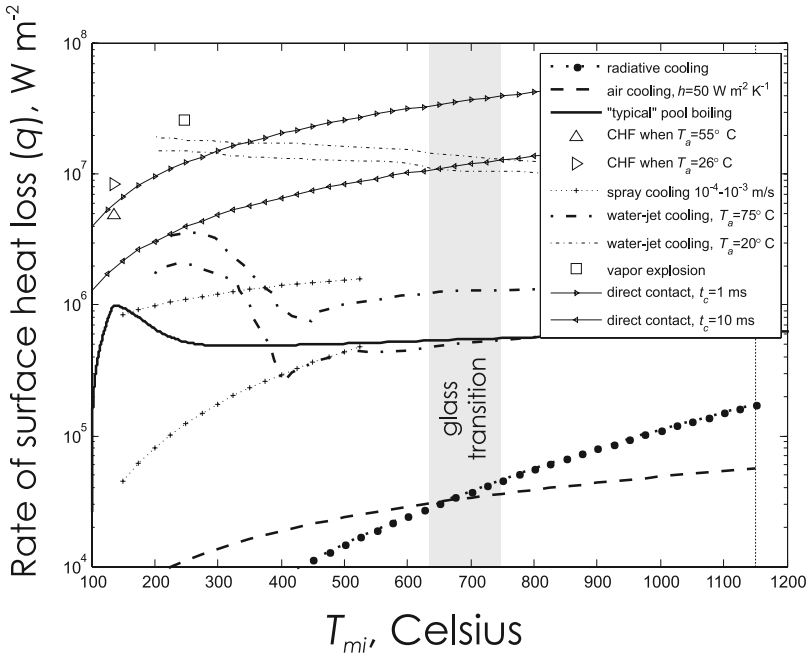

Figure 6. Surface heat flux from hot bodies as a function of their surface temperature at atmospheric pressure. The short-dashed line connected by solid circles represents the curve for radiative cooling using e = 0.75 and T_a = 300 K. Long-dashed line represents surface heat flux for air cooling using h = 50 W m^{-2} K^{-1} and T_a = 300 K. The solid line, taken from Figure 40.1 in the work of *Kreith and Bohn* [1986], represents a typical heat flux curve under saturated pool boiling in which T_a (the water temperature) is at the boiling point (T_b). Up-pointing and right-pointing triangles are critical heat flux values for subcooled water at 55°C and 26°C, respectively, [from *Kreith and Bohn*, 1986, Figure 10.10]. The two thin dotted lines with small crosses bound a range of values for spray cooling under film-boiling conditions, using relations of *Klinzing et al.* [1992]: for low-volumetric flow rates ($Q < 3.5 \times 10^{-3}$ m^3 s^{-1} m^{-2}), $q_{conv}^{spray} = 63.325\ (T_{mi} - T_a)^{1.691}\ Q^{0.264}\ d_{32}^{-0.062}$, where d_{32} is the Sauter mean diameter of droplets; for $Q > 3.5 \times 10^{-3}$ m^3 s^{-1} m^{-2}, $q_{conv}^{spray} = 1.413 \times 10^5\ (T_{mi} - T_a)^{0.461}\ Q^{0.566}\ u^{0.639}$, where u is impact speed of the droplets in m/s. These relations have been calibrated for the range of parameters Q = 0.58–9.96 $\times$ 10^{-3} m^3 s^{-1} m^{-2}, u = 10.1–29.9 m s^{-1}, d_{32} = 0.137 – 1.35 $\times$ 10^{-3} m, T_{mi} < 520°C. The lower curve in this figure uses the low-Q solution for Q = 6 $\times$ 10^{-4} m^3 s^{-1} m^{-2}, T_a = 25°C, and d_{32} = 0.001 m; the upper curve represents the high-Q relation for Q = 1 $\times$ 10^{-2} m^3 s^{-1} m^{-2}, T_a = 25°C, and u = 30 m/s. The bold dot-dashed lines are experimental heat flux relations for an impinging water jet, T_a = 75°C, with impact velocity of 1 m/s (lower curve) to 3 m/s (upper curve) [*Liu and Wang*, 2001, Figure 5a]. Fine dot-dashed lines are experimental heat flux relations for a subcooled water jet impacting at 2 m/s (lower curve) to 6 m/s (upper curve), with water temperature at T_a = 20°C [*Liu and Wang*, 2001, Figure 4]. The square represents the heat flux rate from a jet of molten tin-lead alloy (T = 260–287°C) to water (T_a = 25°C) estimated by *Bradley and Witte* [1972] over the timescale of a vapor explosion (0.2–0.5 ms). The thin solid lines with left-pointing triangles represent average conductive heat flow rates over time periods of 1 ms (upper curve) and 10 ms (lower curve), calculated by the error function solution described in the text. The range of glass transition temperatures, indicated by the shaded box, was estimated for Etna basalt containing 0.02 wt% water, using a best-fit line through viscosity data of *Giordano and Dingwell* [2003]. The best-fit curve has the form $\log_{10}(\mu) = 0.033(10{,}000/T)^3 - 0.47(10{,}000/T)^2 + 3(10{,}000/T) - 7.8$, where T is temperature in Kelvin and μ is the viscosity in Pascal seconds. The left side of the box represents the temperature at which $\mu = 10^{12}$ Pa s; the right side represents the temperature at which the melt fails brittlely under a strain rate ($\dot{\varepsilon}$) of 10 s^{-1}, using the failure criterion $\mu > 0.01G/\dot{\varepsilon}$ [*Dingwell and Webb*, 1989] where G, taken as 2.5 $\times$ 10^{10} Pa, is the Young's modulus of the melt (the modulus extrapolated to infinite frequency under cyclic loading). This range of basalt glass transition temperatures is somewhat lower than the range obtained through calorimetry (e.g., ~870°C in *Wilding et al.* [2000]) but agrees well with the glass transition temperature of Kilauean basalt (T = 900–1000 K) obtained through calorimetry by *Gottsman et al.* [2004].

Table 1. Variables

Symbol	Explanation	Units
c_m	magma specific heat	J kg^{-1} K^{-1}
c_{pw}	specific heat of liquid water at constant pressure	J kg^{-1} K^{-1}
d	droplet diameter	m
d_{32}	Sauter mean droplet diameter	m
e	radiative emissivity	–
G	Young's modulus of melt (modulus of extension extrapolated to infinite frequency under cyclic loading)	Pa
g	gravitational acceleration	m s^{-2}
h	heat transfer coefficient	W m^{-2} K^{-1}
k_m	magma thermal conductivity	W m^{-1} K^{-1}
k_w	thermal conductivity of liquid water	W m^{-1} K^{-1}
L_{11}	integral length scale of turbulent velocity fluctuations	m
Q	volumetric flow rate of sprays (used in Figure 6)	m^3 s^{-1} m^{-2}
q	heat flow rate	W m^{-2}
q_{conv}	rate of convective heat loss	W m^{-2}
q_{conv}^{air}	rate of convective heat loss to air	W m^{-2}
q_{rad}	rate of radiative heat loss	W m^{-2}
$\overline{q}$	average rate of heat loss over a finite time interval	W m^{-2}
R	clast radius	m
$R_{1/2}$	radial distance from center of a self similar jet at which the mean upward velocity equals half the mean upward velocity at the jet centerline	m
r	radial distance from clast center	m
s	mean square of turbulent velocity fluctuations	m^2 s^{-2}
T	Temperature	K or C
T_a	air temperature or temperature of ambient fluid surrounding globules or pyroclasts	K or C
T_b	boiling temperature of water	K or C
T_m	magma temperature	K or C
T_{mi}	temperature at surface of magma or hot body	K or C
t	Time	s
t_b	time required for secondary droplet breakup	s
t_c	time interval over which liquid water is in direct contact with magma	s
t_L	integral timescale of turbulent velocity fluctuations	s
$U(t)$	instantaneous fluid velocity in a jet at time t	m s^{-1}
$\overline{U}$	mean upward velocity of jet at a given location	m s^{-1}
U_0	mean upward velocity of a jet at its centerline	m s^{-1}
u	velocity of droplets	m s^{-1}
u_t	terminal velocity of droplets	m s^{-1}
u_η	characteristic eddy velocity at the Kolmogorov scale	m s^{-1}
z	distance above vent	m
$\dot{\varepsilon}$	extensional strain rate	s^{-1}
ε	rate of turbulent energy dissipation	W kg^{-1}
η	Kolmogorov scale of turbulent velocity fluctuations	m
μ_a	viscosity of air, or of the ambient fluid surrounding pyroclasts or globules	Pa s
κ_m	thermal diffusivity of magma	m^2 s^{-1}
μ_L	viscosity of liquid in a deforming droplet	Pa s
μ_m	viscosity of magma	Pa s
ρ_a	gas density or density of the ambient fluid surrounding pyroclasts or globules	kg/m^3
ρ_L	density of liquid in a globule	kg/m^3
ρ_m	magma density	kg/m^3
ρ_w	density of liquid water	kg/m^3
σ	surface tension between magma and ambient fluid	Pa m
σ_b	Stefan-Boltzmann constant, 5.67×10^{-8} J K^{-4} m^{-2} s^{-1}	J K^{-4} m^{-2} s^{-1}
τ_η	Kolmogorov timescale of turbulent velocity fluctuations	s
τ_t	dynamic pressure gradient across the length of a globule	Pa
$\xi(t)$	a standardized Gaussian random variable whose mean value is 0 and whose variance is 1	–
	Dimensionless Numbers	
Oh_d	Droplet Ohnesorge number $Oh_d \equiv \mu_L/(\rho_L d\sigma)^{1/2}$	
Re_0	Jet Reynolds number $Re_0 \equiv \rho U_0 R_{1/2}/\mu_a$	
We_d	Droplet Weber number $We_d \equiv \rho_a d u^2/\sigma$	

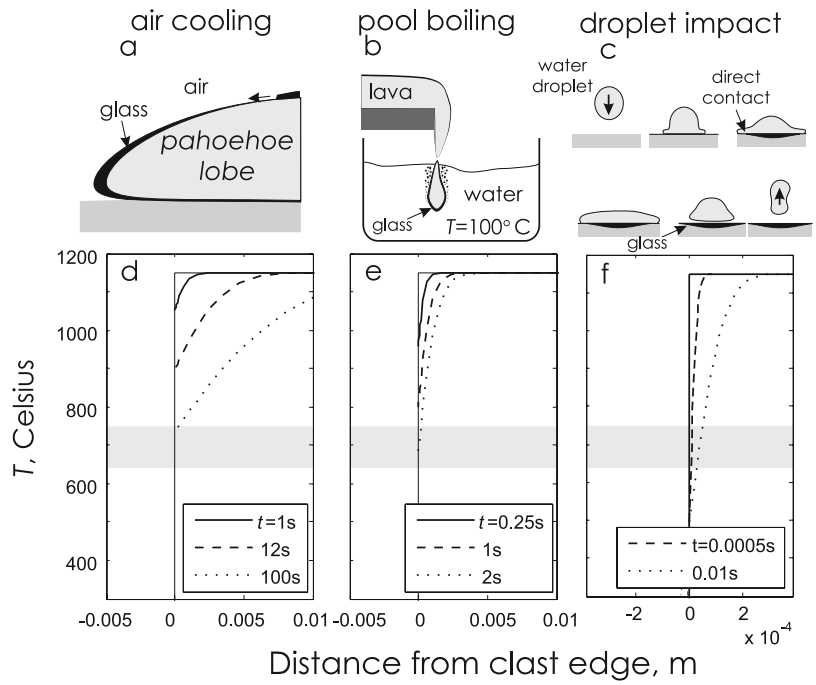

Figure 7. (a–c) Illustration of magma surface cooling under (Figure 7a) air-cooling conditions associated with, for example, subaerial pahoehoe-toe emplacement; (Figure 7b) pool boiling; and (Figure 7c) impact of a water droplet on a magma surface. (d–f) Temperature profiles near a magma surface calculated for (Figure 7d) air cooling, (Figure 7e) water cooling under pool boiling conditions; and (Figure 7f) cooling over the timescale of a single droplet impact. Glass transition temperature range is calculated using the method described in Figure 6. Sequence of diagrams in Figure 6c illustrates the deformation and rebound typically observed when droplets of low Weber number impact surfaces whose temperature lies above the Leidenfrost temperature [*Bernardin et al.*, 1997; *Bolle and Moureau*, 1982]. For droplets of ~1 mm diameter impacting at ~1 m/s, this sequence takes place over several milliseconds.

than 90% of heat is transferred during these first milliseconds.

[24] At the instant of contact, assuming perfect thermal coupling between the magma and water, the temperature at the interface would be given by [*Cronenberg*, 1980]:

$$T_{mi} = \frac{T_w\sqrt{\rho_m c_m k_m} + T_m\sqrt{\rho_w c_{pw} k_w}}{\sqrt{\rho_m c_m k_m} + \sqrt{\rho_w c_{pw} k_w}}, \tag{3}$$

where T_w, ρ_w, c_{pw}, and k_w are the temperature, density, specific heat at constant pressure, and thermal conductivity of liquid water, respectively; T_m, ρ_m, c_m, and k_m are the corresponding properties for magma.

[25] Using ρ_w = 1000 kg m^{-3}, k_w = 0.6 W m^{-1} K^{-1}, c_{pw} = 4.1 kJ kg^{-1} K^{-1}; [*Haar et al.*, 1984]; T_m = 1150°C, and ρ_m = 2400 kg m^{-3}, c_m = 1.3 kJ kg^{-1} K^{-1}, k_m = 1.5 W m^{-1} K^{-1} [*Clauser and Huenges*, 1995; *Spera*, 2000], the interface temperature is about 500°C, which is below the glass transition temperature. Hence an infinitesimally thin layer of glass should form almost immediately and thicken with time. At t = 0, the interface temperature gradient and heat flux are theoretically infinite but decay rapidly to finite values.

[26] Assuming that interfacial temperature doesn't change significantly in the first few milliseconds, the evolution of magma near-surface temperature with position (r) and time (t) can be approximated by [*Carslaw and Jaeger*, 1959, p. 51]:

$$T(r,t) = T_{mi} + (T_m - T_{mi})erf\left[\frac{R-r}{2\sqrt{\kappa_m t}}\right] \tag{4}$$

where *erf* is the error function and κ_m (= $k_m/(\rho_m c_m)$) is the thermal diffusivity of magma. This equation can be used to find the thermal gradient at the boundary (r = R), from which the instantaneous heat flow rate (q) can be calculated:

$$q = -k_m \frac{\partial T}{\partial r}\bigg|_{r=R} \tag{5}$$

The instantaneous heat flux can then be integrated numerically with time and divided by the time of contact (t_c), to give the average heat flow $\overline{q}$:

$$\overline{q} = \frac{1}{t_c}\int_0^{t_c} q\,dt \tag{6}$$

Calculated values of $\overline{q}$ for t_c = 1 and 10 ms (Figure 6, fine solid lines with triangles) range up to several tens of

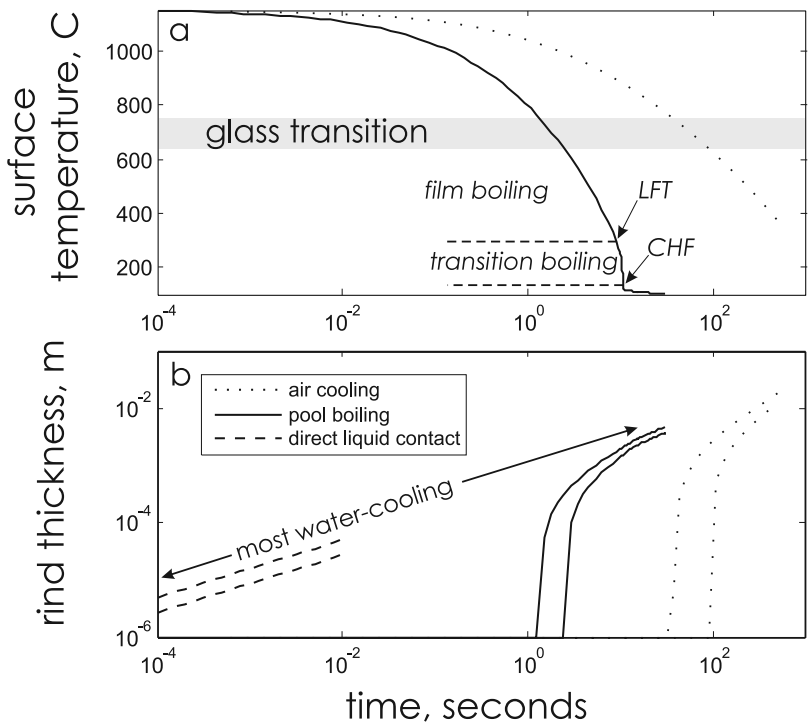

Figure 8. Clast surface temperature (a) and glassy rind thickness (b) versus log time for air cooling (dotted lines) and water cooling (solid lines). For each of these cooling scenarios, Figure 8b shows a range of glassy rind thicknesses bounded by two lines, which represent the range of glass transition temperatures (639–750°C, respectively) shown in Figure 6. Figure 8b also shows glassy rind thickness versus time as a result of direct water contact during droplet impact (dashed lines).

megawatts per square meter—significantly more than most other heat flow rates. Heat flow rates could be still higher if convection reduced the interface temperature below that given by (3). Replacing T_{mi} in (4) with T_a, for example, yields an approximate maximum theoretical heat flow rate which is about twice that obtained from (4) in its present form.

[27] It should be emphasized that cooling rates during direct liquid contact differ substantially from those involving convective or radiative heat loss in that the latter are limited by the rate at which heat can be convected or radiated away whereas the former are limited primarily by the thermal diffusivity of magma. Experimental data in Figure 6 for water jets, subcooled CHF, and vapor explosions (square) exceed theoretical heat flux values for direct liquid magma-water contact over 1–10 ms timescales, but these higher measured rates result in part from the use of metals in these measurements whose thermal conductivities may be tens of times higher than that of magma. For the lead-tin alloy used in vapor explosions reported by *Bradley and Witte* [1972] for example (square in Figure 6), $k = \sim 50-75$ W m^{-1} K^{-1}; for SUS304 stainless steel used in water jet experiments by *Liu and Wang* [2001] (dash-dotted lines, Figure 6), $k = \sim 17$ W m^{-1} K^{-1}, while for magma $k_m = \sim 1.5$ W m^{-1} K^{-1}.

3.4. Calculated Rate of Glassy Rind Growth

[28] In this section we calculate the cooling history near a clast surface by assuming a spherical clast with uniform cooling around its outer surface. For a clast of radius R, the rate of change of temperature (T) with time (t) in the clast interior is:

$$\frac{\partial T}{\partial t} = \frac{k_m}{\rho_m c_m r^2} \frac{\partial}{\partial r}\left(r^2 \frac{\partial T}{\partial r}\right) \tag{7}$$

where r is the radial distance from the clast center. At $t = 0$, the clast is assumed to have a uniform temperature $T_m = 1150$°C. For cooling by convection and (or) radiation, (7) is integrated using the following boundary condition at the clast surface:

$$\left[\frac{\partial T}{\partial r}\right]_{r=R} = -\frac{1}{k_m}[q_{conv} + q_{rad}] \tag{8}$$

[29] Figures 7 and 8 show the temperature-time history of the near-surface clast interior (Figure 7) and the clast surface (Figure 8a), calculated by integrating (7) under conditions of (Figure 7a) air cooling (using h = 50 W m^{-2} K^{-1} and T_a = 25°C) and (Figure 7b) pool boiling (using ρ_m = 2400 kg m^{-3}, c_m = 1.3 kJ kg^{-1} K^{-1}, k_m = 1.5 W m^{-1} K^{-1} [*Clauser and Huenges*, 1995; *Spera*, 2000], and T_m = 1150°C). Also shown (Figure 7f) is the evolution of temperature within a clast over the timescale of a single droplet impact (Figure 7c), calculated using (3) and (4). Figure 8b illustrates the growth in glassy rind thickness with time under air cooling (dotted lines), pool boiling (solid lines), and direct contact of liquid water and melt (dashed lines). The double

lines represent the rind thicknesses that would exist under the range of glass transition temperatures illustrated in Figure 8a.

[30] After about 1–2s of cooling under pool boiling, a glassy rind begins to form on the clast margin (Figure 7e); after several additional seconds the clast surface has cooled below the Leidenfrost temperature ("LFT", Figure 8a), below which vapor explosions are unlikely to occur [*Zimanowski*, 1998]. The thickness of the glassy rind at this time is on the order of a millimeter (Figure 8b) and the thickness of the thermal boundary layer a few additional millimeters (Figure 7e). The rest of the clast remains at its initial temperature (Figure 7e) and is able to deform. Under air-cooling conditions, some tens of seconds are required to form a rind (Figures 7d and 8a); moreover, lower-temperature gradients in the air-cooled magma mean that, once the surface temperature crosses below the glass transition, a glassy rind of several millimeters thickness develops very rapidly (Figure 8b): the zone of cooled melt extends a few centimeters inward of the glassy rind (Figure 7d) and its elevated viscosity inhibits further clast deformation. Temperature curves over the timescale of droplet impact (Figure 7f) produce glassy rind thicknesses of several microns to tens of microns (Figure 8b).

[31] Each of these cooling rates results in the first appearance of a glassy rind at different times, and different characteristic rind thicknesses over the initial period of rind growth. Between the rind thickness curves for direct contact and pool boiling in Figure 8b lies a region occupied by rind growth within subcooled water or under forced convection. The overall range of timescales for the first appearance of glassy rinds by water cooling therefore extends from fractions of a millisecond to at least seconds; initial rind thicknesses range from microns to at least millimeters. Glassy rinds can of course grow longer than these time periods and reach greater thickness if they are not removed during growth.

4. Stripping of Glassy Rinds in Turbulent Flows

[32] Glassy rinds separate or shatter during a variety of eruptive processes, both magmatic and hydromagmatic. Cooling pahoehoe flows emplaced on dry land crackle and ping as millimeter- to centimeter-sized thin glassy rinds pop off their surfaces (M. Mangan, written communication, 2005). In open channels, viscous skins peel away from the incandescent interior as lava goes around bends or through cascades. Rinds on water-cooled lava can be disrupted by an impacting wave or an imploding pillow. On pyroclasts entrained in turbulent jets, cypressoid plumes, or bubble bursts, glassy rinds may be disrupted by the strains and accelerations associated with turbulent velocity fluctuations or by impact with other clasts.

[33] These disruptive events may repeat on a timescale ranging from small fractions of a second for turbulent flows to seconds or longer for wave impact. Here we consider two specific mechanisms associated with such mixing: the breakup of large magma globules during flight ("secondary breakup"); and velocity fluctuations within turbulent jets ("turbulent breakup").

4.1. Secondary Breakup

[34] The breakup of liquid jets up into globules, droplets, and sprays has been extensively studied [e.g., *Lin and Reitz*, 1998; *Liu*, 2000; *Marmottant and Villermaux*, 2004]. In the idealized case, jets are envisioned to exit from a nozzle as an intact cylinder of liquid (such as water coming out of a faucet). In high-speed jets, however, aerodynamic forces combine with gravitational forces to deform the liquid surface and, through Rayleigh-Taylor instabilities, pull it into ligaments that separate from the intact jet to form globules. This process, termed "primary breakup" [*Lin and Reitz*, 1998; *Marmottant and Villermaux*, 2004] is illustrated in Figure 3 ("a").

[35] Globules that result from primary breakup are typically unstable and continue to break up during flight. This process of "secondary breakup" is related to aerodynamic instability, quantified by the Weber number ($We_d = \rho_a d u^2/\sigma$, where d = globule diameter u = globule velocity, σ = surface tension, and ρ_a = ambient fluid density [*Weber*, 1931]). At $We_d = 3.0-13$ globules deform in an oscillatory manner but do not break up (Figure 9). At $We_d = \sim 13-35$, the globule flattens to a disc-like and then to a bag-like shape, opening in the upstream direction, then splits into droplets about an order of magnitude smaller than the initial globule diameter. At $We_d > \sim 80$ [*Hsiang and Faeth*, 1992], droplets flatten and then elongate into a bullet-like shape aimed upstream. Boundary layer drag along the globule's surface causes fluid to migrate toward the trailing edge where Rayleigh-Taylor instabilities form ligaments that separate into small droplets. Continual removal of these trailing droplets reduces the main globule size until it stabilizes. The first breakup mode is termed "bag breakup", the second "shear breakup" [*Hsiang and Faeth*, 1992]. A mixed breakup mode occurs at Weber numbers between about 35 and 80.

[36] In highly viscous liquids, secondary breakup is inhibited because of the resistance of those liquids to deform under stress. The effect of viscosity is represented in Figure 9 through the dimensionless Ohnesorge number $Oh_d \equiv \mu_L/\sqrt{d\rho_L\sigma}$, where μ_L and ρ_L are viscosity and density of the liquid. At $Oh_d < \sim 0.1$ the threshold Weber number for breakup is independent of Oh_d whereas above this value Weber numbers required for breakup become progressively higher. It is generally thought [*Hinze*, 1955; *Hsiang and Faeth*, 1992] that breakup is suppressed at Oh_d not far above 3.5, though the exact limit is unknown; extrapolation of the threshold curves (Figure 9) suggest that breakup is still possible, albeit at much higher Weber numbers, for Oh_d approaching 10. Breakup experiments have been conducted for Oh_d up to about 3.5 [*Hsiang and Faeth*, 1992], which corresponds roughly to the value of basalt globules.

[37] Dashed and dotted bold lines in Figure 9 represent the range of Oh_d and We_d relevant to basalt globules of decimeter to meter size where ρ_L = 1000 kg m^{-3}, σ_L = 0.3 Pa m, μ_L ranges from 20 to 100 Pa s, d ranges from 0.1 to 1.1 m, and u is the terminal velocity (u_t), which is given by [e.g., *Mironer*, 1979, p. 297]:

$$u_t = \sqrt{\frac{4d(\rho_L - \rho_a)g}{3\rho_a C_d}} \tag{9}$$

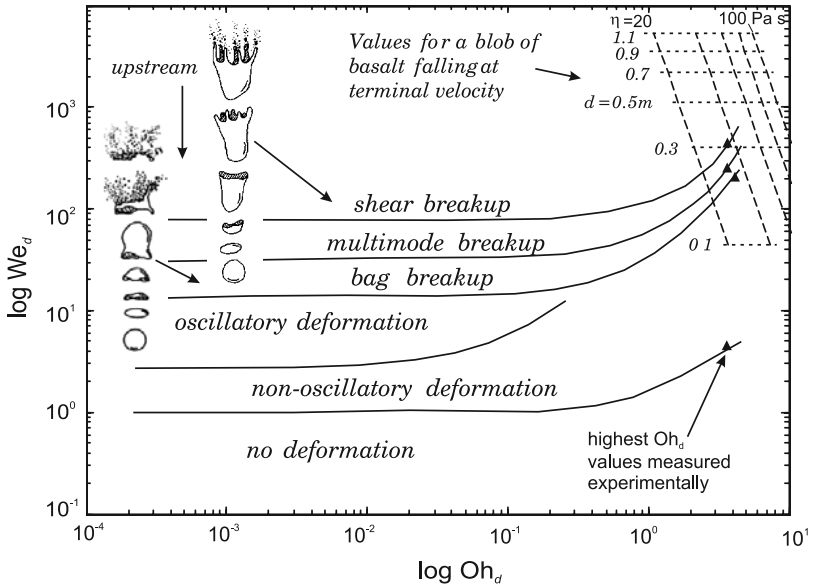

Figure 9. Log Weber number (We_d) versus log Ohnesorge number (Oh_d), showing the range regimes for secondary droplet breakup [from *Hsiang and Faeth*, 1992]. Solid lines show boundaries between various types of breakup regimes; cartoons on the left illustrate the sequence of droplet deformation leading to bag breakup (left) and shear breakup (right). Dashed lines trending from upper left to lower right illustrate the changes in We_d and Oh_d for magma globules of decreasing size and associated terminal velocity (calculated from (9)), holding ρ_L = 1000 kg m^{-3} and σ = 0.3 Pa m constant. Dashed lines represent magma viscosities of (left to right) 20, 40, 60, 80, and 100 Pa s. Dotted lines illustrate the change in Oh_d with increasing viscosity for globules having values of d labeled in the plot, $u = u_t$, and ρ_L = 1000 kg m^{-3}. Dotted lines represent (from bottom to top) globule diameters of 0.1, 0.3, 0.5, 0.7, 0.9, and 1.1 m, respectively. Triangles illustrate the highest values of Oh_d for which experiments of secondary droplet breakup have been conducted [*Hsiang and Faeth*, 1992].

using a drag coefficient (C_d) of 1, which is roughly average for droplets [*Hsiang and Faeth*, 1992]. The result suggests that basalt globules of a few decimeters in diameter or larger, falling at terminal velocity through still air, are subject to shear breakup.

[38] The timescale of breakup and the resulting droplet size are not well characterized for the Oh_d and We_d values relevant to volcanism. For Oh < ~3.5 and We_d < ~10^3, limited experimental data show that the breakup time roughly follows the relation [*Hsiang and Faeth*, 1992]:

$$t_b = \sim \frac{5d(\rho_L/\rho_a)^{1/2}}{u(1 - Oh_d/7)} \tag{10}$$

which gives a breakup time of several seconds to a few tens of seconds for magma globules 0.1–1 m in diameter. Following breakup, the size of daughter droplets decreases with We_d [*Hsiang and Faeth*, 1992]; for the values of We_d considered in Figure 9, mean daughter droplet sizes are likely several times smaller than the original droplets, suggesting that the globules starting at a few meters in diameter or less will undergo a few generations or less of secondary droplet breakup before reaching a stable diameter. If each generation of rind removal coincided with a secondary breakup event, the time between secondary droplet breakup events (several seconds or more) would seem too long, and the number of breakup events too few, to result in rapid, repeated rind removal. Under directly observable conditions such as illustrated in Figure 3, droplet breakup is clearly much faster than these laboratory-scale results indicate.

4.2. Turbulent Breakup

[39] Turbulent flows such as the continuous uprush jets at Surtsey have velocities (U_0) in the core of the jet exceeding 100 m/s [*Thorarinsson*, 1967] and basal diameters of tens of meters [*Kokelaar*, 1987] to more than 100 m [*Moore*, 1985]. Assuming the viscosity of the fluid surrounding pyroclasts (μ_a) to roughly equal that of air (~1 × 10^{-5} Pa s) and the mixture density (ρ = ~10 kg m^{-3}) to be about an order of magnitude greater than air (~1.2 kg m^{-3}), Reynolds numbers ($Re_0 \equiv \rho U_0 R_{1/2}/\mu_a$) should exceed 10^8 (where $R_{1/2}$ is the radial distance from the jet centerline to the point at which the mean upward velocity equals one half U_0). The high Reynolds number implies that kinetic energy is transferred through turbulent eddies down to very small scale and that turbulent velocity fluctuations are high in amplitude. In the core of a self-similar turbulent jet, the root mean square of turbulent velocity fluctuations is typically ~25–30% of the mean centerline velocity [*Pope*, 2000, p. 100], implying velocity fluctuations within a continuous uprush jet of tens of meters per second.

[40] Figure 10 shows synthetic plots, calculated using the Ornstein-Uhlenbeck method described in the caption [*Pope*, 2000, equation (12.90); *Wyganski and Fiedler*, 1969], that have the approximate magnitude and frequency distribution

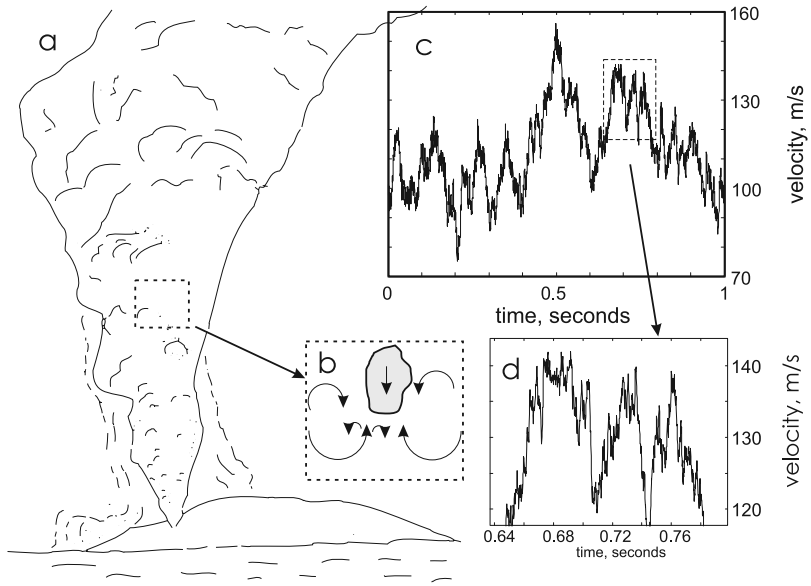

Figure 10. Illustration of the turbulent velocity fluctuations in a Surtseyan continuous uprush jet. Within the jet (a), magma globules (b) are falling at terminal velocity at the same time that they are being buffeted by eddies. For a steady, self-similar jet having a mean centerline velocity (U_0) of 100 m/s and radius ($R_{1/2}$) of 50 meters (defined as the distance from the jet center at which the velocity reaches $^1/_2$ U_0), Figures 10c and 10d are simulations that illustrate the approximate amplitude and frequency distribution of velocity fluctuations. The plots were generated using an Ornstein-Uhlenbeck process [*Pope*, 2000, equation (12.90)] for a Lagrangian particle within a statistically stationary turbulent flow. The plots are calculated using the formula [*Pope*, 2000, equation (12.90)] $U(t+\Delta t) = U(t) - \left(U(t) - \overline{U}\right)\frac{\Delta t}{t_L} + \left(\frac{2s^2\Delta t}{t_L}\right)^{1/2}\xi(t)$ where $U(t)$ is the instantaneous velocity at time t, $\overline{U}$ is the mean flow velocity (taken as 100 m/s), Δt is an increment of time (taken in this case to be the Kolmogorov timescale), t_L is the integral timescale of turbulent velocity fluctuations (taken as L_{11}/U_0 = 20m/100 m/s = 0.2 s), s is the root mean square of turbulent velocity fluctuations (taken as 25 m/s), and $\xi(t)$ is a standardized Gaussian random variable whose mean value is 0 and whose variance is 1.

of velocity fluctuations in such a jet. In the core of the jet, fluctuations of tens of meters per second can occur over less than a tenth of a second. Velocity fluctuations include relatively long period excursions lasting more than ~0.1 s and brief fluctuations ranging down to the Kolmogorov timescale $\tau_\eta \equiv (\mu_a/(\rho_a\varepsilon))^{1/2}$ [*Kolmogorov*, 1941], where ε is the rate of turbulent energy dissipation (W/kg), which is roughly $0.017U_0^3/R_{1/2}$ = 340 W/kg near the jet centerline [*Wyganski and Fiedler*, 1969]. For values U_0, $R_{1/2}$, and μ_a noted above and ρ_a = 1 kg/m^3, the Kolmogorov timescale is about 1×10^{-4} s. Velocity fluctuations in Figures 10c–10d represent the passage of turbulent eddies of different sizes.

[41] The characteristic size and velocity range of such eddies are well characterized in self-similar turbulent jets [e.g., *Hussein et al.*, 1994; *Pope*, 2000, chapter 5; *Wyganski and Fiedler*, 1969]. The largest eddies correspond roughly to the integral length scale (L_{11}), the scale over which the velocity structure is statistically coherent, which is about $0.4R_{1/2}$ = ~20 m near the jet centerline [*Wyganski and Fiedler*, 1969]. The smallest eddies occur roughly at the Kolmogorov scale [*Kolmogorov*, 1941]:

$$\eta = \left(\frac{\mu_a^3}{\rho_a^3\varepsilon}\right)^{1/4} \tag{11}$$

which is ~10^{-5} m in this case. The characteristic eddy velocity at this scale ($u_\eta = (\varepsilon\mu_a/\rho_a)^{1/4}$) is ~$10^{-1}$ m/s.

[42] *Hinze* [1955] proposed that that turbulent globule breakup is most strongly affected by velocity gradients over a distance equal to the dimension of a globule. The dynamic pressure gradient across this distance is

$$\tau_t = \frac{1}{2}\rho_a\Delta U^2 \tag{12}$$

where ΔU^2 is the difference in the square of the velocity across the length of the globule. The parameter τ_t can be regarded as a tensile stress causing the clast to deform. Figure 11 illustrates the velocity difference $U(t+\Delta t) - U(t)$ calculated from the simulation in Figure 10, for time differences (Δt) ranging from the Kolmogorov timescale to roughly 0.2 s. Assuming that globules are falling at their terminal velocity relative to the mean jet velocity, the globule diameter over which these velocity fluctuations would act would be $d \approx u_t\Delta t$. Tick marks showing values of d corresponding to the given values of Δt are shown at the top of Figure 11. Globules with diameters of centimeters to meters are most likely to break up as a result of velocity

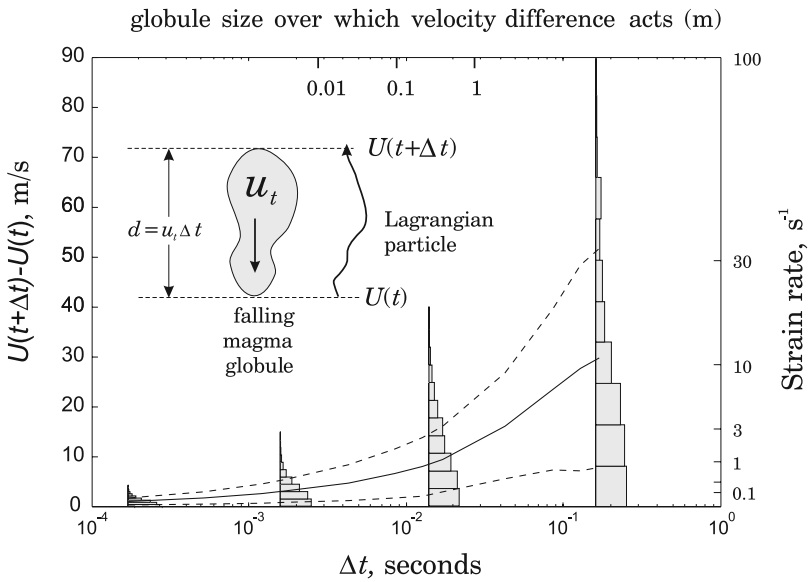

Figure 11. Differences in velocity U calculated over finite time intervals Δt from the synthetic turbulent velocity fluctuations shown in Figure 10. The solid line represents the mean velocity difference; dashed lines are located one standard deviation above and below the mean. Rotated histograms on the plots illustrate the range of velocity differences measured at Δt values of 2×10^{-4}, 2×10^{-3}, 2×10^{-2}, and 0.02 s. The values of $U(t + \Delta t) - U(t)$ represent the differences in velocity between times t and $t + \Delta t$ of a Lagrangian particle in a turbulent flow (inset) and are assumed to be the velocity difference ΔU across a magma globule falling at its terminal velocity u_t and having a dimension $d = u_t \Delta t$. For a given value of Δt, tick marks on the top of the plot give corresponding values of d for a given Δt and a value of u_t determined from (9). On the right-hand side of the plot are strain rates that correspond to a given value of $U(t + \Delta t) - U(t)$, calculated as explained in the text.

fluctuations over timescales of a few milliseconds to about 0.1 s.

[43] For globule diameters of $d = \sim 0.01-1$ m, mean velocity differences acting across the globule diameter (solid line in Figure 11) are roughly 5–15 m/s, though maximum values for the 1-second simulation are about 15–75 m/s. When used in (12), such velocity differences imply maximum tensile stresses of 10^2-10^3 Pascals. Extensional strain rates of globules subject to these stresses would be roughly τ_t/μ_m; assuming μ_m = 50 Pa s (typical of Kilauean basalt at T = 1150°C [*Shaw*, 1972]) and ρ_a = $\sim$1 kg m^{-3}, the extensional strain rate for a given velocity difference is calculated from (12) and plotted as tick marks on the right-hand side of Figure 11. The result indicates that decimeter-sized globules are consistently subjected to strain rates of 1 s^{-1} by the fluctuating velocity field and likely exceed 10 s^{-1} several times per second. The extensional strain accumulated over a fraction of a second vastly exceeds that required ($\sim 10^{-4}$ [*Varshneya*, 1994, chapter 18]) to fracture the glassy rinds that form over this timescale under moderate to high rates of heat loss.

[44] The estimated rates of strain and globule breakup for this particular case should be regarded as conservative. The fluid density used in these calculations (1 kg m^{-3}) corresponds approximately to ambient air; higher fluid density (ρ_a) associated with water vapor or water sprays in (12) translates to increased dynamic pressure and greater deformation rates. Particle impacts which are also neglected could raise short-term strain rates by at least an order of magnitude.

5. Conclusions

[45] The growth and removal of glassy rinds can be directly observed at Kilauea and inferred from the surface features on littoral pyroclasts. Calculated cooling rates suggest that glassy rinds $10^{-6}-10^{-3}$ m thick form in a fraction of a second in the presence of water, and that, in turbulent flows having the intensity of Surtseyan jets, disturbances that remove or disintegrate such rinds may occur over the same timescale. These results suggest that turbulent shedding is a viable mechanism for generating fine hydromagmatic tephra in cases where mixing is turbulent and water is present; in littoral jets, bubble bursts, Surtseyan cypressoid plumes, continuous uprush events and in the expansion phase of vapor explosions. The mechanism of turbulent shedding requires primarily that the timescale of glassy rind growth be comparable to the timescale over which clasts are deforming and breaking apart. If the size of blocky, equant hydroclasts is comparable to the thickness of glassy rinds at the time of disintegration, then very fine ($<\sim 100$ μm) hydroclasts suggest very thin rinds, associated most likely with high cooling rates and timescales of rind growth of $10^{-1}-10^{-4}$ s (Figure 8). The low end of this range corresponds to the detonation timescale of laboratory-generated vapor explosions [*Zimanowski et al.*, 1997b]

while the high end is within the range of velocity fluctuations in jets (e.g., Figure 10d).

[46] Like *Zimanowski et al.* [1997b] and *Buettner et al.* [1999], we conclude that the finest blocky fragments are those that were in direct contact with water on clast margins. Moreover, like *Wohletz* [1983] we infer that small blocky pyroclasts result primarily from near-simultaneous brittle fracture and quenching, and that fluid instabilities associated with turbulent mixing produce fine ash. This study differs from those earlier ones primarily in emphasizing that fine fragments result not only from thermal detonation but also from high deformation and cooling rates that may be associated with jetting or other nonexplosive turbulent processes.

[47] The presence of partially detached glassy rinds <100 μm thick on littoral clasts (Figure 4) suggest that even these less violent water-magma interactions can produce fine ash. The fact that fine ash composes a small fraction of littoral deposits may result from the extremely brief period ($<\sim 1$ s) over which littoral lava was subject to high deformation and cooling rates. By contrast, high strain and cooling rates in large Surtseyan jets may persist for tens of seconds to minutes. Blocks ejected at 100 m/s for example reach a theoretical maximum height of $(1/2)U_0^2/g = 700$ m in 35 seconds, and fall back in an equal amount of time, allowing time for hundreds of generations of rind growth and disintegration.

[48] Outside of the context of vapor explosions, few experiments have studied relationships between hydromagmatic fragment size and rates or durations of cooling and deformation. Hydromagmatic ash generated in steady or transient jets under controlled laboratory conditions could be usefully compared with that produced in discrete vapor explosions. Also of value would be field examination of clast morphology and grain size distribution under mixing conditions where turbulence intensity, duration, and the presence or absence of discrete explosions, can be constrained. Finally, in cases where fragmentation results from repeated shedding in jets rather than from impulsive fragmentation in explosions, it may be possible to find systematic variations in grain size, vesicularity and dissolved water content that reflect evolving conditions [e.g., *Mastin et al.*, 2004]. It is hoped that this paper's results will stimulate more rigorous investigation of this process.

[49] **Acknowledgments.** I wish to thank Jane Takahashi for use of the spectacular photo in Figure 3. Thorough reviews were provided by Margaret Mangan, Laszlo Keszthelyi, Ken Wohletz, an anonymous reviewer, and *Journal of Geophysical Research* Associate Editor Jim Gardner. Ken Wohletz's extensive comments, oral discussions, and patient advice greatly added to the quality of this paper.

References

Abtahi, A. A., A. B. Kahle, E. A. Abbott, A. R. Gillespie, D. Sabol, G. Yamada, and D. Pieri (2002), Emissivity changes in basalt cooling after eruption from Pu'u O'o, Kilauea, Hawaii, *Eos Trans. AGU*, *83*(47), Fall Meet. Suppl., abstract V71A-1263.

Bernardin, J. D., and I. Mudawar (1997), Film boiling heat transfer of droplet streams and sprays, *Int. J. Heat Mass Transfer*, *40*, 2579–2593.

Bernardin, J. D., C. J. Stebbins, and I. Mudawar (1997), Mapping of impact and heat transfer regimes of water drops impinging on a polished surface, *Int. J. Heat Mass Transfer*, *40*, 247–267.

Board, S. J., C. L. Farmer, and D. H. Poole (1974), Fragmentation in thermal explosions, *Int. J. Heat Mass Transfer*, *17*, 331–339.

Board, S. J., R. W. Hall, and R. S. Hall (1975), Detonation of fuel coolant explosions, *Nature*, *254*, 319–321.

Bolle, L., and C. Moureau (1982), Spray cooling of hot surfaces, in *Multiphase Science and Technology*, edited by G. F. Hewitt et al., pp. 1–92, Taylor and Francis, Philadelphia, Pa.

Bradfield, W. S. (1966), Liquid solid contact in stable film boiling, *IEC Fundam.*, *5*, 200–204.

Bradley, R. H., and L. C. Witte (1972), Explosive interaction of molten metals injected into water, *Nucl. Sci. Eng.*, *48*, 387–396.

Buchanan, D. J. (1974), A model for fuel-coolant interaction, *J. Phys. Dev. Appl. Phys.*, *7*, 1441–1457.

Buchanan, D. J., and T. A. Dullforce (1973), Mechanism for vapour explosions, *Nature*, *245*, 32–34.

Buettner, R., and B. Zimanowski (1998), Physics of thermohydraulic explosions, *Phys. Rev. Lett.*, *57*, 5726–5729.

Buettner, R., P. Dellino, and B. Zimanowski (1999), Identifying magma-water interaction from the surface features of ash particles, *Nature*, *401*, 688–690.

Buettner, R., P. Dellino, L. L. Volpe, V. Lorenz, and B. Zimanowski (2002), Thermohydraulic explosions in phreatomagmatic eruptions as evidenced by the comparison between pyroclasts and products from molten fuel coolant interaction experiments, *J. Geophys. Res.*, *107*(B11), 2277, doi:10.1029/2001JB000511.

Burgi, P., M. Caillet, and S. Haefeli (2002), Field temperature measurements at Erta'Ale lava lake ethiopia, *Bull. Volcanol.*, *64*, 472–485.

Carslaw, H. S., and J. C. Jaeger (1959), *Conduction of Heat in Solids*, 2nd ed., 510 pp., Clarendon, Oxford, U. K.

Clauser, C., and E. Huenges (1995), Thermal conductivity of rocks and minerals, in *Rock Physics and Phase Relations: A Handbook of Physical Constants*, edited, pp. 105–126, AGU, Washington, D. C.

Colgate, S. A., and T. Sigurgeirsson (1973), Dynamic mixing of water and lava, *Nature*, *244*, 552–555.

Corradini, M. L. (1991), Vapor explosions: A review of experiments for accident analysis, *Nucl. Safety*, *32*, 337–362.

Cronenberg, A. W. (1980), Recent developments in the understanding of energetic molten fuel-coolant interactions, *Nucl. Safety*, *21*, 319–337.

Dingwell, D. B., and S. L. Webb (1989), Structural relaxation in silicate melts and non-Newtonian melt rheology in geologic processes, *Phys. Chem. Miner.*, *16*, 508–516.

Fisher, R. V., and H.-U. Schmincke (1984), *Pyroclastic Rocks*, 472 pp., Springer, New York.

Giordano, D., and D. B. Dingwell (2003), Viscosity of hydrous Etna basalt: Implications for Plinian-style basaltic eruptions, *Bull. Volcanol.*, *65*, 8–14.

Gottsmann, J., A. J. L. Harris, and D. B. Dingwell (2004), Thermal history of Hawaiian pahoehoe lava crusts at the glass transition: Implications for flow rheology and emplacement, *Earth Planet. Sci. Lett.*, *228*, 343–353.

Haar, L., J. S. Gallagher, and G. S. Kell (1984), *NBS/NRC Steam Tables*, 320 pp., Taylor and Francis, Philadelphia, Pa.

Heiken, G. (1972), Morphology and petrography of volcanic ashes, *Geol. Soc. Am. Bull.*, *83*, 1961–1988.

Hinze, J. O. (1955), Fundamentals of the hydrodynamic mechanism of splitting in dispersion processes, *AIChE J.*, *1*, 289–295.

Hon, K., C. Heliker, and J. I. Kjargaard (1988), Limu o Pele: A new kind of hydroclastic tephra from Kilauea Volcano, Hawaii, paper presented at Geological Society of America, 1988 National Meeting, Denver, Colo.

Hsiang, L. P., and G. M. Faeth (1992), Near-limit drop deformation and secondary breakup, *Int. Multiphase Flow, J.*, *18*, 635–652.

Hussein, H. J., S. P. Capps, and W. K. George (1994), Velocity measurements in a high-Reynolds-number momentum-conserving, axisymmetric, turbulent jet, *J. Fluid Mech.*, *258*, 31–75.

Kahle, A. B., A. R. Gillespie, E. A. Abbott, M. J. Abrams, R. E. Walker, G. Hoover, and J. P. Lockwood (1988), Relative dating of Hawaiian lava flows using multispectral thermal infrared images: A new tool for geologic mapping of young volcanic terranes, *J. Geophys. Res.*, *93*, 15,239–15,251.

Keszthelyi, L., and A. Harris (2003), Observations of the effect of wind on the cooling of active lava flows, *Geophys. Res. Lett.*, *30*(19), 1989, doi:10.1029/2003GL017994.

Klinzing, W. P., J. C. Rozzi, and I. Mudawar (1992), Film and transition boiling correlations for quenching of hot surfaces with water sprays, *J. Heat Treating*, *9*, 91–103.

Kokelaar, B. P. (1987), Discussion of "Structure and eruptive mechanisms at Surtsey Volcano, Iceland" by J. G. Moore, *Geol. Mag.*, *124*, 79–86.

Kolmogorov, A. N. (1941), The local structure of turbulence in incompressible viscous fluid for very large Reynolds numbers, *Dokl. Akad. Nauk SSSR*, *30*, 299–303.

Kreith, F., and M. S. Bohn (1986), *Principles of Heat Transfer*, 700 pp., HarperCollins, New York.

Lin, S. P., and R. D. Reitz (1998), Drop and spray formation from a liquid jet, *Annu. Rev. Fluid Mech.*, *30*, 85–105.

Liu, H. (2000), *Science and Engineering of Droplets*, 527 pp., Noyes Publ., Park Ridge, N. J.
Liu, Z.-H., and J. Wang (2001), Study on film boiling heat transfer for water jet impinging on high temperature flat plate, *Int. J. Heat Mass Transf.*, *44*, 2475–2481.
Marmottant, P., and E. Villermaux (2004), On spray formation, *J. Fluid Mech.*, *498*, 73–111.
Mastin, L. G., R. L. Christiansen, C. Thornber, J. Lowenstern, and M. Beeson (2004), What makes hydromagmatic eruptions violent? Some insights from the Keanakako'i Ash, Kilauea Volcano, Hawai'i, *J. Volcanol. Geotherm. Res.*, *137*, 15–31.
Mattox, T. N., and M. T. Mangan (1997), Littoral hydrovolcanic explosions: A case study of lava-sea water interaction at Kilauea Volcano, *J. Volcanol. Geotherm. Res.*, *75*, 1–17.
Mironer, A. (1979), *Engineering Fluid Mechanics*, 592 pp., McGraw-Hill, New York.
Moore, J. G. (1967), Base surge in recent volcanic eruptions, *Bull. Volcanol.*, *30*, 337–363.
Moore, J. G. (1985), Structure and eruptive mechanisms at Surtsey Volcano, Iceland, *Geol. Mag.*, *6*, 649–661.
Morimoto, R. (1960), Submarine eruption of the Myojin reef, *Bull. Volcanol.*, *23*, 151–160.
Morrissey, M. M., B. Zimanowski, K. Wohletz, R. Buettner, and R. D. Ballard (2000), Phreatomagmatic fragmentation, in *Encyclopedia of Volcanoes*, edited by H. Sigurdsson et al., pp. 431–445, Elsevier, New York.
Patel, P. D., and T. G. Theofanus (1978), Fragmentation requirements for detonating thermal explosions, *Nature*, *274*, 142–144.
Peckover, R. S., D. J. Buchanan, and D. E. T. F. Ashby (1973), Fuel-coolant interactions in submarine volcanism, *Nature*, *245*, 307–308.
Pope, S. B. (2000), *Turbulent Flows*, Cambridge Univ. Press, New York.
Richards, A. F. (1959), Geology of the Islas Revillagigedo, Mexico, 1. Birth and development of Volcan Barcena, Isla San Benedicto (1), *Bull. Volcanol.*, *22*, 73–123.
Salisbury, J. W., and D. M. D'Aria (1994), Emissivity of terrestrial materials in the 3–5 μm atmospheric window, *Remote Sens. Environ.*, *47*, 345–361.
Sharma, A., H. Jain, J. O. Carnali, and I. H. Jain (2003), Inhomogeneous evolution of a glass surface via free, rapid expansion, *Appl. Phys. Lett.*, *83*, 2802–2804.
Shaw, H. R. (1972), Viscosities of magmatic silicate liquids: An empirical method of prediction, *Am. J. Sci.*, *272*, 870–893.
Sheridan, M. F., and K. H. Wohletz (1983), Hydrovolcanism: Basic considerations and review, *J. Volcanol. Geotherm. Res.*, *17*, 1–29.
Spera, F. J. (2000), Physical properties of magmas, in *Encyclopedia of Volcanoes*, edited by H. Sigurdsson et al., pp. 171–190, Elsevier, New York.
Thorarinsson, S. (1967), *Surtsey–The new island in the North Atlantic*, 47 pp., Penguin Group (USA), New York.
Trigila, R., and M. Battaglia (2003), The role of magma porosity in explosive magma-water interaction, *Eos Fall Meeting Supplement*, *84*, Abstract VB51-06.
Varshneya, A. K. (1994), *Fundamentals of Inorganic Glasses*, 570 pp., Elsevier, New York.
Walker, G. P. L. (1971), Grain-size characteristics of pyroclastic deposits, *J. Geol.*, *79*, 696–714.
Walker, G. P. L., and R. Croasdale (1972), Characteristics of some basaltic pyroclasts, *Bull. Volcanol.*, *35*, 303–317.
Waters, A. C., and R. V. Fisher (1971), Base surges and their deposits: Capelinhos and Taal volcanoes, *J. Geophys. Res.*, *76*, 5596–5613.
Weber, C. (1931), Zum Zerfall eines Flussigkeitstrahles, *Z. Angew. Math. Mech.*, *11*, 136–159.
Wilding, M., D. B. Dingwell, R. Batiza, and L. Wilson (2000), Cooling rates of hyaloclastites: Applications of relaxation geospeedometry to undersea volcanic deposits, *Bull. Volcanol.*, *61*, 527–536.
Witte, L. C., T. Cox, and J. E. Bouvier (1970), The vapor explosion, *J. Metals*, *22*, 39–44.
Wohletz, K. H. (1983), Mechanisms of hydrovolcanic pyroclast formation: Grain-size, scanning electron microscopy, and experimental studies, *J. Volcanol. Geotherm. Res.*, *17*, 31–63.
Wohletz, K. H. (1986), Explosive magma-water interactions: Thermodynamics, explosion mechanisms, and field studies, *Bull. Volcanol.*, *48*, 245–264.
Wohletz, K. H., and R. G. McQueen (1984), Experimental studies of hydromagmatic volcanism, in *Explosive Volcanism: Inception, Evolution, and Hazards*, edited by F. R. Boyd et al., pp. 158–169, Natl. Acad. Press, Washington, D. C.
Wohletz, K. H., M. F. Sheridan, and W. K. Brown (1989), Particle size distributions and the sequential fragmentation transport theory applied to volcanic ash, *J. Geophys. Res.*, *94*, 15,703–15,721.
Wyganski, I., and H. Fiedler (1969), Some measurements in the self-preserving jet, *J. Fluid Mech.*, *38*, 577–612.
Zimanowski, B. (1998), Phreatomagmatic explosions, in *From Magma to Tephra: Modeling Physical Processes of Explosive Volcanic Eruptions*, edited by A. Freundt and M. Rosi, pp. 25–53, Elsevier, New York.
Zimanowski, B., G. Fröhlich, and V. Lorenz (1991), Quantitative experiments on phreatomagmatic explosions, *J. Volcanol. Geotherm. Res.*, *48*, 341–348.
Zimanowski, B., G. Froehlich, and V. Lorenz (1995), Experiments on steam explosion by interaction of water with silicate melts, *Nucl. Eng. Design*, *155*, 335–343.
Zimanowski, B., R. Buettner, and V. Lorenz (1997a), Premixing of magma and water in MFCI experiments, *Bull. Volcanol.*, *58*, 491–495.
Zimanowski, B., R. Buettner, V. Lorenz, and H.-G. Haefele (1997b), Fragmentation of basaltic melt in the course of explosive volcanism, *J. Geophys. Res.*, *102*, 803–814.

L. G. Mastin, Cascades Volcano Observatory, U. S. Geological Survey, 1300 SE Cardinal Court, Vancouver, WA 98683, USA. (lgmastin@usgs.gov)